

Received 18 October 2024; revised 30 October 2024; accepted 5 November 2024. Date of publication 7 November 2024;
date of current version 15 November 2024. The review of this article was arranged by Associate Editor X. Yu.

Digital Object Identifier 10.1109/OJNANO.2024.3494544

Portable and Cost-Effective Handheld Ultrasound System Utilizing FPGA-Based Synthetic Aperture Imaging

WENPING WANG  AND ZILIANG FENG 

National Key Laboratory of Fundamental Science on Synthetic Vision, Sichuan University, Chengdu 610065, China

CORRESPONDING AUTHOR: ZILIANG FENG (e-mail: fengziliang@scu.edu.cn).

ABSTRACT The handheld ultrasound has been widely applied in various clinical applications due to its high portability and cost-effectiveness advantages. The smaller hardware architecture can expand its range of application scenarios. However, miniaturized ultrasound devices face the challenges in terms of image quality, frame rate, and power consumption. The achievement of high-quality and high-frame-rate imaging depends on numerous channels and higher pulse repetition frequency (PRF) at the cost of power consumption. The proposed work aims to design a field-programmable gate array (FPGA)-based prototype with synthetic aperture method for portable and cost-effective handheld ultrasound system. The prototype supports 8 transmit and receive channels and forms up to 8 synthetic apertures. In addition, to optimize the FPGA resources, the auto delay calculation and segmented apodizations are employed for 4 parallel beamforming lines. To evaluate the performance of our proposed prototype, scan sequences of B-mode, C-mode, and D-mode are implemented for image construction. The results show that the proposed prototype can provide a lateral resolution of 0.30 mm, a contrast-to-noise ratio (CNR) of 7.58 dB, and a frame rate of 22 frames per second (FPS) in dual-mode imaging. Moreover, it is remarkable that the memory and logic resources in the FPGA (EP4CE55) account for 73.7% and 66.2%, respectively, which makes the FPGA's power consumption only about 530 mW. The proposed prototype is suitable for handheld and other miniaturized ultrasound imaging systems.

INDEX TERMS Handheld ultrasound, field-programmable gate array (FPGA), synthetic aperture, parallel beamforming, power consumption.

I. INTRODUCTION

Handheld ultrasound device has been widely used in multiple clinical fields, such as point-of-care diagnostics [1], [2], visual guidance [3], [4], preliminary screening [5], and emergency examination [6]. The demand for handheld ultrasound device is driven by the necessity for rapid response with compact design and diagnostic accuracy with high quality image in resource-constrained environments. Miniaturized ultrasound devices will also expand the field of diagnosis and monitoring, providing more clinical application possibilities, especially in the integration with robotic manipulators for autonomous diagnosis or in the integration with wearable transducer for monitoring [7], [8], [9].

However, the design of handheld ultrasound system faces a significant tradeoff between image quality and power consumption. An increased number of channels can enhance

image resolution and contrast, but it also leads to higher power consumption and larger device size, both of which negatively impact the device's portability. Conversely, reducing the number of channels to decrease power consumption may compromise image quality, thereby posing challenges in achieving diagnostic accuracy. To obtain high-quality ultrasound images, many improvements on image processing have been proposed. One type is image-based method, which involves adjusting the gray-level mapping with histogram equalization method or selecting speckle noise suppression algorithm for better contrast images [10], [11]. Another type is deep-learning-based method, which involves transferring low-quality images to high-quality images based on huge amount of dataset with different deep neural networks, such as super-resolution convolutional neural network (SRCNN) [12], motion compensation and residual net (MCResNet) [13], a

low-rank representation multi-pathway generative adversarial network (LLR MPGAN) [14] and so on.

Although these image-based methods have demonstrated some effectiveness, there is still considerable scope for enhancement in signal processing. Techniques such as multi-channel beamforming, multi-beam processing, and multi-angle spatial compounding can greatly enhance the signal-to-noise ratio (SNR) and contrast. High-performance processors are crucial for parallel processing of channel data to achieve high-quality ultrasound images. The utilization of application-specific integrated circuits (ASICs) provides a customized solution that effectively manages power consumption and computational complexity. However, ASIC development is often associated with lengthy design cycles and high upfront costs, limiting their flexibility for rapid prototyping and algorithmic innovation [15]. Graphics processing units (GPUs), while powerful in parallel computing, introduce complexity in hardware integration and pose challenges in managing power consumption in portable devices [16]. Field-programmable gate arrays (FPGAs) present an attractive alternative for prototyping and implementing novel ultrasound imaging techniques. The reconfigurable logic, abundant memory resources, and efficient parallel processing capabilities enable rapid development and optimization of complex algorithms while maintaining low power consumption [17]. Several studies based on different processors have been investigated on the handheld device [18]. Implementations of single-mode scanning in handheld ultrasound systems, such as Doppler mode (D-mode) for blood velocity estimation, have been implemented in single/multi-processor devices. The market has seen the introduction of several commercial handheld ultrasound devices with multiple-mode scanning, such as brightness mode (B-mode) and color mode (C-mode), but most of them are based on ASIC architecture and feature amounts of channels, which makes them inflexible and still cost-prohibitive [19], [20], [21], [22].

The synthetic aperture method presents a promising solution for handheld ultrasound systems aiming to achieve high-quality imaging with limited resources [23]. By employing time-multiplexing to leverage multiple receive apertures from a limited number of physical channels, the synthetic aperture method enhances the effective aperture size, thereby augmenting spatial resolution without necessitating an increase in the physical dimensions of the transducer array. This time-multiplexing approach necessitates efficient beamforming algorithms within the FPGA, which rely heavily on large amounts of random access memory (RAM) for storing delays and apodization coefficients associated with the point-by-point focusing process [24], [25]. However, the constraints imposed by miniaturization and cost reduction necessitate innovative strategies to optimize RAM usage without compromising image quality [26], [27], [28].

In this work, we present a portable and cost-effective FPGA-based handheld ultrasound system that employs synthetic aperture method to balance image quality, frame rate,

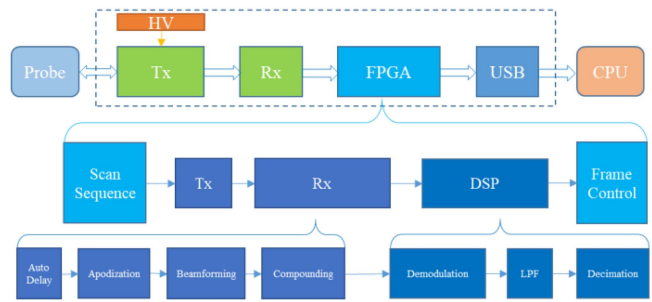


FIGURE 1. The prototype block diagram of the hardware architecture and FPGA processing system.

and power consumption. Our system features eight transmit-receive (Tx-Rx) channels, configurable aperture to achieve up to 64-channel receive focusing, thereby addressing the tradeoffs between image resolution and power consumption. To mitigate the RAM requirements for beamforming, we introduce an optimized strategy that automatically calculates delays and employs segmented apodizations, significantly reducing the dynamic RAM footprint and further contributing to a low-power design. This novel architecture demonstrates the potential of FPGAs in enabling rapid prototyping and optimization of ultrasound imaging techniques for handheld devices, ultimately advancing the frontiers of portable medical imaging.

This article is structured as follows. Section II surveys the works related to scan sequence, Rx, and digital signal processing (DSP) of our proposed prototype. In Section III, data acquisition, performance, and FPGA resource analysis are presented. The results obtained by the different compounding strategies are given in Section IV. Discussion is provided in Section V. And the conclusion is presented in Section VI.

II. METHODS

A. HARDWARE DESCRIPTION

The block diagram of the proposed prototype, as illustrated in Fig. 1, comprises a transmit (Tx) module with high voltage (HV), a receive (Rx) module, an FPGA module and a universal serial bus (USB) module.

The interconnection between the Tx module and the probe enables individual control over array elements, facilitating precise focused transmission. Subsequently, the echo signals are subject to analog amplification and digital sampling by an analog-front-end (AFE) chip in the Rx module. The sampled channel data then flows into the FPGA for processing and it is transferred to the central processing unit (CPU) via a USB interface for further analysis and image display.

Within the FPGA processing system, the scan sequence logic governs the aperture's positioning to achieve precise timing control for each individual Tx-Rx operation. The Tx module controls the transmit waveforms and transmit delays to achieve emission of various frequencies and focusing at different positions. The Rx module automatically calculates delays and applies apodization to execute the delay-and-sum

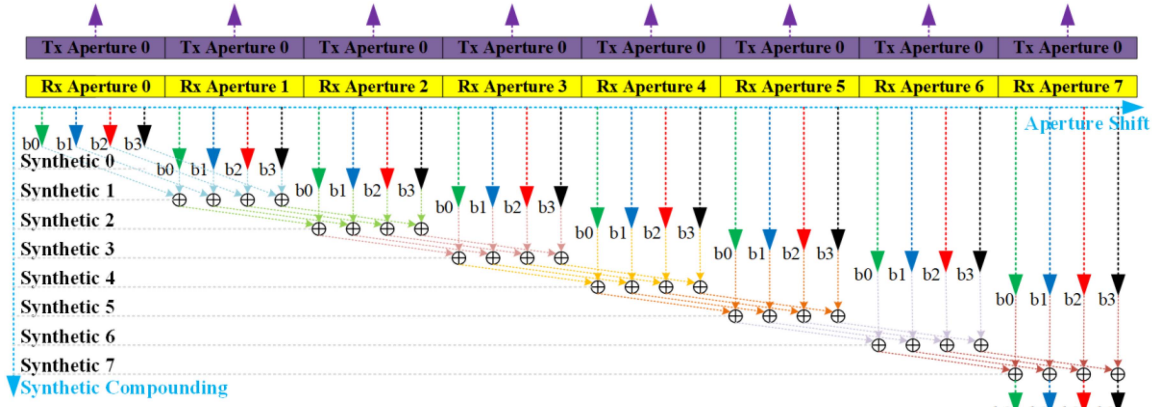


FIGURE 2. The diagram of Tx aperture and Rx synthetic aperture control in one scan sequence. The Tx beam (purple arrow) is generated by the same Tx aperture 0, while different Rx apertures from 0 to 7 are switched to receive the four lines: b0 (green arrow), b1 (blue arrow), b2 (red arrow), and b3 (black arrow). These four lines are then synthetically compounded to complete the process of beamforming.

algorithm for beamforming. Subsequently, the compounding module integrates the beams acquired from different apertures to complete a synthetic aperture compounding process, yielding beamformed scan lines. The scan lines then undergo demodulation, low-pass filter (LPF), and decimation in the digital processing system (DSP) module to generate In-phase and Quadrature (IQ) signals. Finally, the frame control logic facilitates the uploading of IQ signals for further analysis and image display.

B. SCAN SEQUENCE

The system comprises of eight independent transmit and receive channels, indicating that each transmit aperture and receive aperture encompasses eight channels. During one scan sequence, the system initiates transmission through transmit aperture 0, configuring delay and wave parameters to generate the sound field. Subsequently, the system switches to the receive aperture 0, completing data reception and performing parallel 4-line (b0/b1/b2/b3) beamforming. Then, keep the transmit aperture 0, switch to the receive aperture 1, repeat the above operations, and complete one more beamforming operation to add up with the previous 4-line for synthetic compounding. The termination of one scan sequence is determined by the required number of apertures/channels, which can range from 1-aperture/8-channel to 8-aperture/64-channel in our proposed prototype, as illustrated in Fig. 2. The more the times of synthetic apertures, the longer the required time for consumption, while multi-line beamforming can compensate for the time resolution.

The scan sequence module implemented in our proposed prototype supports a total range of 2048 scan times, with each sequence containing 64-bit Tx-Rx control parameters, accommodating various imaging modes. The Tx module is responsible for configuring waveform patterns with different frequencies and cycles, as well as setting 16-bit Tx delays across 8 channels. In order to accommodate the transmit delay of 8 groups, the receiving 4-line module requires a total of

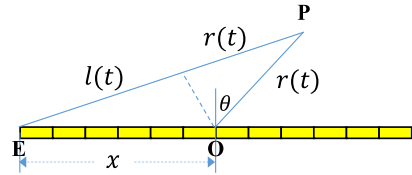


FIGURE 3. Time-of-flight geometry of a linear transducer array. $r(t)$ is the distance from the center position O to the focal point P with steer angle θ . x is the distance from O to the element position E. $l(t)$ is the distance difference from P to both O and E.

32 groups, each with a maximum of 64 channels for receive delay.

C. RX BEAMFORMING

In conventional dynamic receive beamforming, the receive delay and apodization needs to be calculated point-by-point for the purpose of enhancing the consistency of receive beams and improving spatial resolution. One approach to handle delays and apodizations is precomputing the values and storing them in a lookup table, which requires a significant amount of external memory. In order to reduce the complexity of the system, our approach involves employing an on-chip computation method which utilizes iterative algorithms to reduce computational complexity for delays and a segmented method to minimize storage space for apodizations.

1) AUTO DELAY

The time-of-flight, as illustrated in Fig. 3, from the center of the transmitting aperture O to the focal point P, and then back to the receiving element E, can be represented as:

$$l(t) = \sqrt{r^2(t) + 2 \cdot r(t) \cdot x \cdot \sin \theta + x^2} - r(t) \quad (1)$$

where $r(t)$ is the distance from the center position O to the focal point P with steer angle θ , and x is the distance from O to the element position E. Assuming that the speed of sound is c and the sampling frequency of the system is f_s , the sampling period and interval are $T_u = 1/f_s$ and $d = c \cdot T_u/2$,

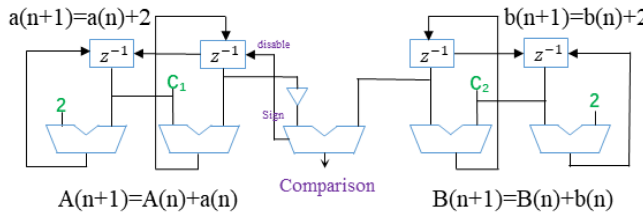


FIGURE 4. Iterative delay calculation in the FPGA algorithm implementation.

respectively. Let $r(n \cdot T_u)/d = n$, the discrete beamforming delay $l(t)$ after n sampling cycles can be represented as $k(n) = l(n \cdot T_u)/d$. (1) can be represented as:

$$\frac{k^2(n) + 2 \cdot k(n) \cdot n + n^2}{A(n)} = \frac{n^2 + \alpha \cdot n + \beta}{B(n)} \quad (2)$$

where $\alpha = 2 \cdot x \cdot \sin \theta/d$ and $\beta = x^2/d^2$.

The terms A and B can be calculated iteratively as:

$$\begin{aligned} A(n+1) &= A(n) + a(n) = A(n) + 2 \cdot n + 2 \cdot k(n) + 1 \\ B(n+1) &= B(n) + b(n) = B(n) + 2 \cdot n + \alpha + 1 \end{aligned} \quad (3)$$

When the initial values $a(0) = 2 \cdot k(0) + 1$ and $b(0) = \alpha + 1$, The changes in $k(n)$ can be detected by a comparison of A and B, where $a(n)$ and $b(n)$ are arithmetic sequence with difference 2:

$$\begin{aligned} a(n+1) &= a(n) + 2 \\ b(n+1) &= b(n) + 2 \end{aligned} \quad (4)$$

This iterative delay calculation method, as illustrated in Fig. 4, requires fewer adder stages in the FPGA algorithm implementation.

For the reception delay of each channel, only the initial number of delay cycles and angle values need to be defined, and the following delay value of the channel at that time can be calculated through the iterative calculation method. The proposed prototype only requires initial parameters α and β for 64-channels, resulting in significant on-chip storage space savings compared to the look-up table (LUT) method. The Rx delay module implemented in our proposed prototype supports a total range of 32 groups for different steer angles or focus depths, while each initial parameter α and β coefficient occupies 16 bits.

2) APODIZATION

The receive apodizations need to be stored point-by-point for the better suppression of sidelobes according to a constant F-number ($F_{\#} = F/D$), which is defined as the ratio of the focusing depth to aperture size, as illustrated in Fig. 5(a).

In theory, the multi-line acquiring requires an independent apodization for each line, resulting in a significant demand for on-chip storage space, as illustrated in Fig. 5(a). The apodization coefficients utilized by adjacent beams exhibit similarity based on their central positions, thereby facilitating the combined apodizations for four lines into one apodization array employing expanded lateral coefficients, as illustrated in

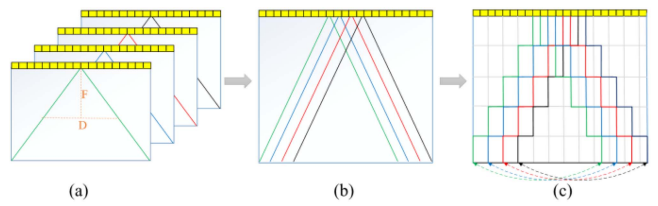


FIGURE 5. Four apodization arrays for four lines (a), one combined apodization for four lines (b), and one segmented apodization for four lines (c).

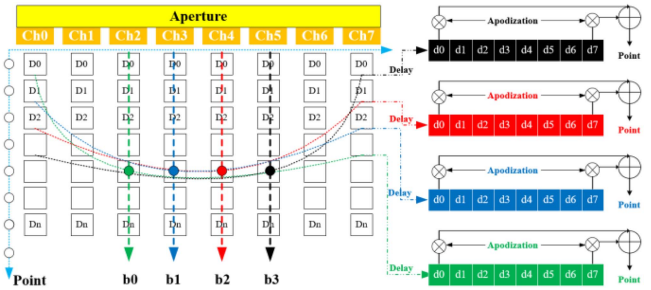


FIGURE 6. Four apodization arrays for four lines (a), one combined apodization for four lines (b), and one segmented apodization for four lines (c).

Fig. 5(b). As the sampling depth increases, aperture expansion occurs in stages, which further reduces the storage space, as illustrated in Fig. 5(c). The proposed prototype divides the Rx depth into 16 sections and expands the aperture with total 72 channels, while each apodization coefficient occupies 16 bits.

3) BEAMFORMING AND COMPOUNDING

The parallel 4-line beamforming with one receive aperture, as illustrated in Fig. 6, necessitates each 8-channel to employ four different delays and apodizations for summing. A RAM with 512-depth and 21-bit width is allocated for 8 channels and 4 lines to achieve delay process in the beamforming module. After delay and apodization, the four radio-frequency (RF) lines are designed to accumulate based on the number of apertures. The proposed prototype supports a maximum number of 10240 sampling points for each line, while each sampling point occupies 16 bits.

D. DIGITAL SIGNAL PROCESSING

As the ultrasound travels through human tissues, the center frequency of the reflected echo signal shifts with increased propagation depth. To achieve greater agility in obtaining signals at the central frequency, a dynamic demodulation method using LUT is designed. Afterwards, the LPF is used to eliminate the aliasing. Subsequently, the demodulated baseband signals are decimated to extract the IQ signals, as illustrated in Fig. 7.

The proposed prototype supports IQ demodulation of 10240 samples, with each IQ coefficient occupying 16 bits. It also enables dynamic filtering operation using 32-group Finite Impulse Response (FIR) filters with symmetrical 64 orders, where each FIR coefficient occupies 16 bits.

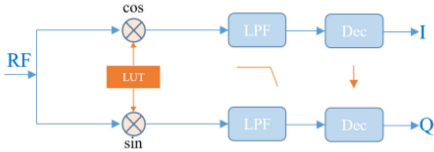


FIGURE 7. DSP module from RF signals to IQ signals.

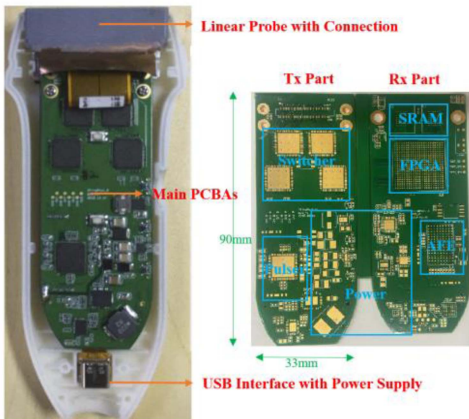


FIGURE 8. The prototype for handheld ultrasound system with linear probe.

III. EXPERIMENTS

Fig. 8 shows the printed circuit board assembly (PCBA) of the portable prototype for a handheld ultrasound device with a linear probe, main PCBA (Tx part and Rx part with back-to-back structure), and a USB interface which is also responsible for supplying power to the system. An eight-layer PCB with a size of 90 x 33 mm includes Tx part and Rx part, as depicted on the right of Fig. 8. The Tx module, which includes four switchers (HDL6M06531B) and one pulser (HDL6M5584), is designed on the Tx part with one PCB. The Rx module, which includes one AFE (AFE5805), two SRAMs, and one FPGA (EP4CE55), is designed on the Rx part with another PCB. This separate design not only ensures the quality of analog signals but also allows for effective adaptation and upgrades to different transducer array elements or physical forms.

A. DATA ACQUISITION

To evaluate the effectiveness of our proposed prototype, experiments with different scan sequences to obtain datasets through the ultrasound system were designed. The datasets processed by FPGA (Intel Corporation, SCV, MA, USA) are transferred to CPU through USB, and the data processing, analysis and image display were processed by Matlab (The Mathworks, Inc., Natick, MA, USA).

The excitation with a center frequency 7.0 MHz was sequentially activated with eight-channel aperture on a linear array consisting of 128 elements. The scattered echo signals were sampled at a frequency of 40 MHz. The transducer and configuration parameters are listed in Table 1.

The scan sequence, Tx, Rx, and DSP module were implemented in Intel FPGA with Verilog HDL on Quartus prime

TABLE 1. Linear-Array & Configuration Parameter Values

| Parameter | Value |
|--------------------|----------|
| Sound speed | 1540 m/s |
| Element number | 128 |
| Element pitch | 0.3 mm |
| Transmit frequency | 7.0 MHz |
| F number | 1.5 |
| Sampling rate | 40.0 MHz |

TABLE 2. FPGA Resource Utilization Summary

| Module | Logic Cells | Memory Bits | DSP18x18 |
|----------------|-------------|-------------|----------|
| Scan Sequence | 416 | 131072 | / |
| Tx | 579 | 1024 | / |
| Rx-Delay | 7988 | 65536 | / |
| Rx-Apodization | 48 | 18432 | 8 |
| Rx-Beamforming | 7963 | 344064 | / |
| Rx-Compounding | 4011 | 655360 | 3 |
| DSP-IQ | 299 | 327680 | 4 |
| DSP-LPF | 11386 | 32768 | 128 |
| Others | 8448 | 10240 | / |
| Total | 41138 | 1586176 | 143 |

17.1. The resources and power performances of FPGA were evaluated by Fitter Resource Utilization and Power Analyzer Tool, respectively.

B. PERFORMANCE

The resolution was assessed by measuring the lateral full-width-at-half-maximum (FWHM, in mm) of the point spread function (PSF) for point scatters.

The contrast was assessed by measuring the contrast-to-noise ratio (CNR, in dB), which quantify the disparity between the target and background. The CNR is defined as:

$$CNR = 20 \log_{10} \left(\frac{|\mu_t - \mu_b|}{\sqrt{(\sigma_t^2 + \sigma_b^2)/2}} \right), \quad (5)$$

where μ_t , μ_b , σ_t and σ_b denote the means and variances of the intensity in both the target and background regions.

C. FPGA RESOURCES

The capabilities of Logic Cells, Memory Bits, and DSP 18x18 resources are essential for providing the versatility and performance necessary to address a diverse range of digital and signal processing challenges. The utilization of the primary resources is presented in Table 2.

The utilization of Logic Cells, Memory Bits, and DSP 18x18 resources in our proposed prototype implemented on the FPGA (EP4CE55) account for 73.7% (41138 / 55856), 66.2% (1586176 / 2396160), and 92.9% (143 / 154), respectively.

IV. RESULTS

The portable and configurable architecture of the proposed prototype provides opportunities for multiple imaging modes.

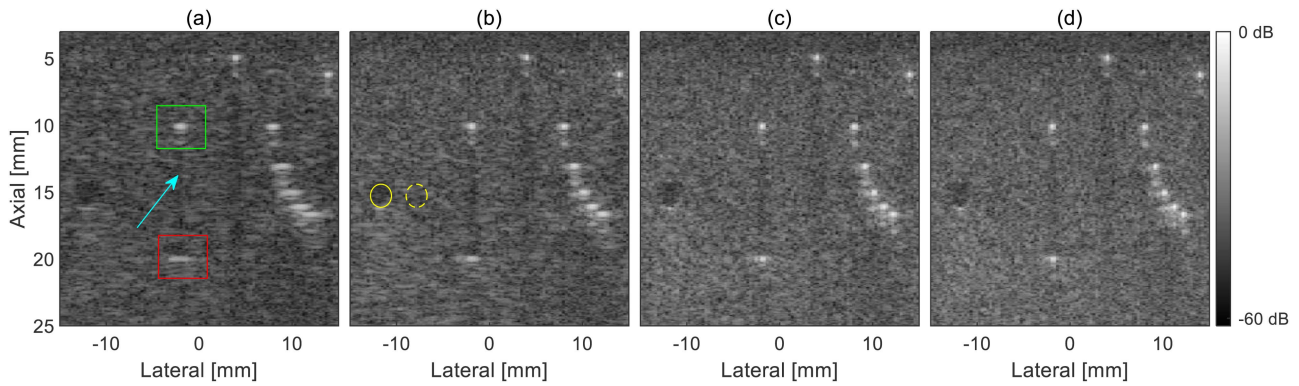


FIGURE 9. B mode images using one aperture (a), two apertures (b), four apertures (c), and eight apertures (d). The point scatters within green and red boxes in (a) are used to compute the FWHMs in the lateral direction. The regions with solid and dashed yellow circles in (b) are used to compute the CNR. The blue arrow in (a) indicate the acoustic shadow. Images are logarithmically compressed with a dynamic range of 60 dB.

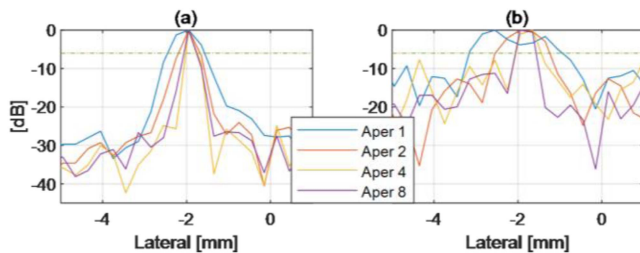


FIGURE 10. Comparisons of lateral resolution at depths of 10 mm (a) and 20 mm (b) with different apertures ranging from 1 to 8.

In this section, imaging scans with B-mode, D-mode, and C-mode were designed in linear system by configuring different scan sequences.

A. B-MODE

For the B-mode scan sequence, which requires spatial resolution, one Tx aperture, and various Rx synthetic aperture numbers are employed to achieve high-resolution imaging for comparison. The image reconstructed by 128 scan lines are formed through the 4 lines during 32 Tx times, with synthetic apertures ranging from 1 to 8. The B-mode images of point scatters and anechoic cyst reconstructed by different apertures numbers are illustrated in Fig. 9.

As the number of aperture increases from 1 to 8, it can be observed that both resolution and contrast are improved. Specifically, in terms of resolution, the lateral resolution of the point at a depth of 10 mm (green box) is better than that of the point at a depth of 20 mm (red box). With the increase in aperture size, the lateral resolution of points at different depths is enhanced, with a more pronounced improvement observed at deeper depths, as illustrated in Fig. 10.

Quantitative measurements of FWHMs in lateral directions at depths of 10 mm and 20 mm are computed in Table 3. As the number of aperture increases from 1 to 8, the lateral resolutions at depth of 10/20 mm are improved from 0.84/2.22 mm to 0.30/0.48 mm. In terms of contrast, with the increase in aperture size, the anechoic cyst exhibits increasing contrast. Quantitative measurements of CNR is computed in Table 3.

TABLE 3. Quantitative Measurements of FWHMs and CNR

| Apertures/Channels | 1/8 | 2/16 | 4/32 | 8/64 |
|-----------------------------|------|------|------|------|
| FWHM _{Z=10mm} (mm) | 0.84 | 0.55 | 0.31 | 0.30 |
| FWHM _{Z=20mm} (mm) | 2.22 | 1.32 | 0.60 | 0.48 |
| CNR(dB) | 5.22 | 6.31 | 7.51 | 7.58 |

As the number of aperture increases from 1 to 8, the CNR is improved from 5.22 dB to 7.58 dB.

B. DOPPLER MODE

For the D-mode scan sequence, which requires temporal resolution, single-aperture is employed to achieve high-frame-rate motion imaging with only one output line for beamforming. First, the vascular localization needs to be located through B-mode image, then the sampling volume (SV) within the vessel needs to be selected, as illustrated in Fig. 11(a). An angle (+5°) of steered sound beam is adjusted to provide a better presentation of blood flow velocity. At a pulse repetition frequency (PRF) of 5 kHz, the maximum blood flow velocity detected is about 28 cm/s. By performing envelope analysis on the spectrogram, as illustrated in Fig. 11(b), the heart rate is estimated to be approximately 73.6 beats per minute (BPM).

For the C-mode scan sequence, the B-mode image is essential for vascular localization, and a region-of-interest (ROI) box is selected in the flow area, as illustrated in Fig. 12(a). However, unlike D-mode, which scans only in a one-dimensional position, multiple scans are performed to calculate the Doppler shift in a two-dimensional ROI region. The 64 scan lines within the ROI are generated by combining the data from 4 lines over a span of 16 Tx times, with one synthetic apertures for high-frame-rate. Each scan line is repeated 12 times for flow velocity calculation with auto-correlation method at the Tx frequency of 5 MHz, and then overlaid with a color map onto the B-mode image for display, as illustrated in Fig. 12(b).

The C-mode imaging requires both B scan sequences for localization and C scan sequences for velocity calculation, and the dual-modality mode that includes both scan sequences has a crucial impact on the frame rate of the imaging. The PRF not

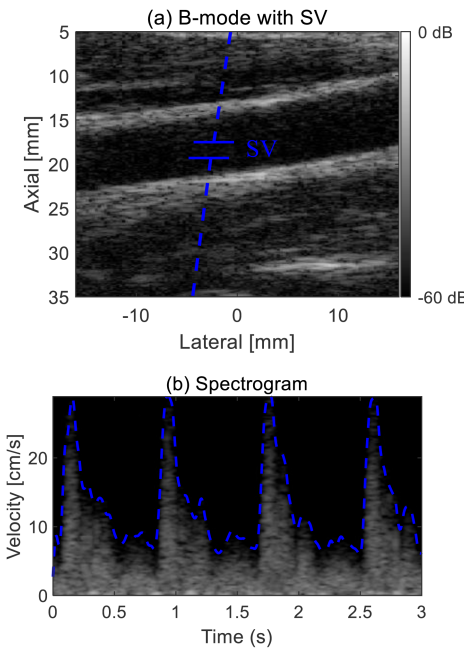


FIGURE 11. Vascular localization in B-mode image with SV (a) and spectrogram of D-mode image (b).

TABLE 4. System Frame Rate Comparison

| Mode | Line Number | Aperture Number | Multi-Line | Frame Rate |
|------|---------------|-----------------|------------|------------|
| B | 128 | 1 | 1/2/4 | 39/78/156 |
| | | 8 | 1/2/4 | 5/10/20 |
| C | 128(B)+768(C) | 1(B)+1(C) | 1/2/4 | 6/11/22 |
| | | 4(B)+1(C) | 1/2/4 | 4/8/16 |

only affects the imaging frame rate but also the range of blood flow velocity selection. Therefore, it is beneficial to trade off at different depths and frame rates to achieve higher-quality images through the proposed flexible configuration prototype.

C. FRAME RATE

Due to the influence of aperture synthesis on imaging time resolution, the proposed prototype enables different combinations of aperture numbers and multi-line numbers to be adopted in various applications for optimizing spatial-time resolution. For instance, as illustrated in Table 4, a detailed comparison is conducted when PRF = 5 kHz (corresponding to the maximum detectable depth of 15.4 cm).

In B-mode, increasing the aperture when the scan line number is determined to be 128 results in a reduction in frame rate. However, the implementation of multi-line parallel reception technology can effectively mitigate this impact, enabling a frame rate of 20 frames per second (FPS) through the utilization of eight apertures for four-line reception. In C-mode, dual-mode scanning is employed, with B scan lines set at 128 and C scan lines set at 768. The frame rate can reach 22 FPS when the B and C scan using 1 aperture with four-line parallel reception. The image quality of the background B-mode image can be enhanced by increasing the number of

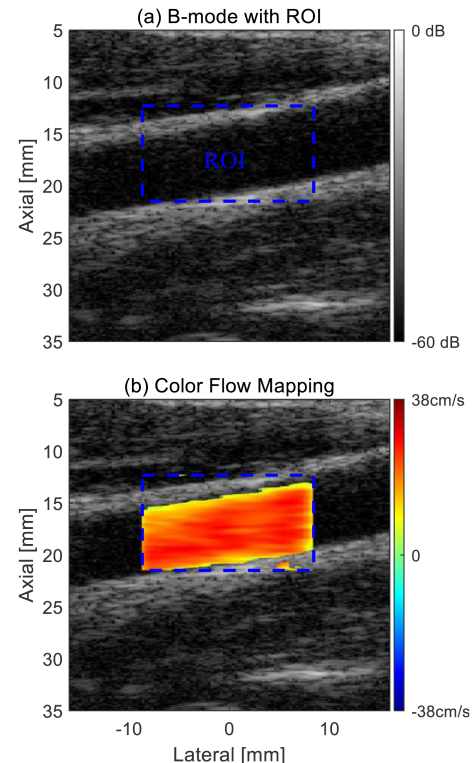


FIGURE 12. Vascular localization in B-mode image with ROI (a) and color flow mapping of C-mode image (b).

B-scan aperture. By increasing the aperture to 4, it can achieve a frame rate of 16 FPS with four-line parallel reception. In D-mode, the maximum temporal resolution is determined by the PRF when a single-aperture is used in the scan sequence for blood flow detection.

D. POWER CONSUMPTION

Variations in imaging modes result in different power consumption due to the varying number of selected transmit cycles when at a PRF of 5 kHz and a bipolar high voltage of ± 50 V. The number of transmit cycles for B-mode, C-mode, and D-mode are 2, 4 and 8, respectively. A digital 64-channel LightProbe model proposed in [29] is compared with respect to FPGA and overall system power consumption, operating at a PRF of 4.9 kHz and a bipolar high voltage of ± 50 V. The power consumption comparison between the proposed prototype and LightProbe model is indicated in Table 5.

V. DISCUSSION

The proposed FPGA-based prototype is designed for a portable and cost-effective handheld ultrasound system. It aims to provide high-quality and high-frame-rate images by using synthetic aperture techniques in different application scenarios. Specifically, the 8-channel Tx and Rx modules are implemented on two back-to-back PCBAs. The Tx module is responsible for generating pulses at the corresponding positions of acoustic window, while the Rx module is tasked with receiving and digitizing echo signals. The digital RF

TABLE 5. System Power Dissipation Summary and Comparison

| Module | Proposed Prototype Power(mW) | LightProbe Model Power(mW) |
|--------------|---------------------------------|-------------------------------|
| Tx | 920(B)/1440(C)/2160(D) | 2150 |
| Rx | 990 | 4400 |
| FPGA-Total | 530 | 1800 |
| FPGA-Tx | 21 | - |
| FPGA-Rx | 210 | - |
| FPGA-DSP | 83 | - |
| FPGA-Others | 216 | - |
| Total | 2440(B)/2960(C)/3600(D) | 8350(B) |

signals from different channels are then processed by an automatic delay algorithm and a segmented apodization design to achieve parallel beamforming of four lines. Finally, the IQ signal after beamforming is transferred to the host computer via a USB module for processing and display in various modes.

In terms of resolution, as the number of synthetic aperture increases, the lateral resolution will improve. The lateral resolution of scatter at a depth of 10 mm in the green box, as illustrated in Fig. 9(a), is enhanced from 0.84 mm to 0.31 mm with an increase in aperture from 1 to 4 (corresponding to an increase in channel number from 8 to 32). However, when the aperture further increases to 8 (channel number increases to 64), the lateral resolution remains consistent at 0.30 mm. This is related to the F-number being set at 1.5, and the lateral resolution no longer changes when the channel number reaches 22. The blue arrow in Fig. 9(a) indicates that the scatter below will create a certain level of acoustic shadow due to intense reflection, thereby impacting the vertical imaging of other positions. The overall trend of the lateral resolution change remains consistent at a depth of 20 mm in the red box. Increasing the channel number will reduce the impact of acoustic shadow on imaging, as depicted in Fig. 10(b). In terms of contrast, with the increase in aperture, the CNR of the anechoic cyst increases by 2.36 dB, and its boundary also becomes clearer.

The evaluation of ultrasound systems necessitates the consideration of not only spatial resolution and contrast, but also temporal resolution, which serves as a crucial indicator. The B-mode can achieve a frame rate of 20 FPS with optimal image quality, while the C-mode can reach a frame rate of 22 FPS for high-speed detection when PRF = 5 kHz. Therefore, the inclusion of configurable Tx and Rx delays is necessary in Doppler mode, a requirement that our proposed prototype adequately satisfies through its provision of 8 Tx delay groups and 32 Rx delay groups. By combining different PRF, scan sequences, and multi-line strategies, various functions can be accomplished under different imaging modes to fulfill the requirements of many clinical applications effectively.

Compared to the commercialized Lumify (Philips) and IQ+ (Butterfly) handheld ultrasound devices, the proposed prototype demonstrates comparable lateral resolution in the near field as shown in Table 6. Additionally, B-mode imaging can achieve over 20 FPS for temporal resolution while C-mode imaging can reach 20 FPS, which is equivalent to IQ+'s

TABLE 6. Resolution and Frame Rate Comparison

| Device | Proposed Prototype | Lumify L12-4 | Butterfly IQ+ |
|------------------------------|--------------------|-------------------|----------------|
| FWHM _{lateral} (mm) | 0.30 | 0.30 | 0.38 |
| Frame Rate(FPS) | 20(B) 16~22(C) | 23(B) 10~16(C) | 22(B) 21(C) |

21 FPS and superior to Lumify's 16 FPS [30], [31]. These findings provide a strong foundation for clinical application of the proposed prototype.

In terms of power consumption, this discrepancy primarily stems from the high voltage and transmit pulser components of the Tx module. Conversely, the power consumption of the digital module such as Rx, FPGA, and USB remains constant. Specifically, the power consumption of FPGA is only about 530 mw, while the Rx consumes approximately 990 mW, resulting in a total digital end power consumption of 1420 mW. In the LightProbe model, the power consumption of FPGA required for processing of 64 digital channels amounts to 1800 mW. As the number of physical channels for Tx and Rx increases, the overall system power consumption also rises to 8350 mW, which poses challenges in achieving more compact ultrasound devices. The higher power consumption from Tx/Rx to FPGA has led most commercial handheld devices to adopt ASIC architecture in order to mitigate its impact. The proposed design has significantly enhanced power efficiency on FPGA. The primary source of power consumption in this system is attributed to the Tx part. The overall power consumption reaches 2440 mW when emitting two pulsers, and it will increase to 3600 mW as the number of pulses increases. The USB Type C interface can provide a maximum power supply capacity of about 5 W, which adequately supports various imaging modes within this system.

It is worth noting that, although the synthetic aperture method is employed at the Rx module to achieve multi-channel beamforming, the Tx module suffers from a limited number of channels and a small transmitting aperture, resulting in a low SNR of the acoustic field. Consequently, this adversely affects both resolution and contrast of the image. To address this issue, our proposed prototype adopts a separate Tx-Rx structure which allows for future scalability by upgrading to additional Tx channels based on demands.

In this study, we present a portable and cost-effective handheld ultrasound system based on an FPGA architecture that employs the synthetic aperture method. By configuring various scan sequences, different ultrasound imaging modalities can be implemented. Additionally, the balance between image quality, frame rate, and power consumption can be customized to meet the requirements of specific clinical applications. This approach greatly lowers both the development complexity and cost of the handheld ultrasound device. In the future work, we aim to improve voltage conversion efficiency of the HV power module or potentially integrating new transducers based on micro-electro-mechanical systems (MEMS) [32], such as piezoelectric micromachined ultrasonic transducer

(PMUT) or capacitive micromachined ultrasonic transducer (CMUT) [33], [34]. This highly portable ultrasound imaging architecture, with low energy consumption and superior imaging capabilities, is not only suitable for handheld devices but also possible for long-term monitoring and wearable ultrasound applications.

VI. CONCLUSION

In this paper, we propose a portable and cost-effective FPGA-based architecture for handheld ultrasound system. To our knowledge the proposed prototype is the minimum eight-channel system for high quality ultrasound imaging with synthetic aperture method. Various scan sequences are employed to reconstruct images and the results show that the resolution, contrast, and frame rate can fulfill different clinical applications with B-mode, C-mode, and D-mode. In addition, the proposed prototype performs lower power consumption and FPGA resources with auto delay calculation and segmented apodization. In conclusion, the proposed prototype can provide benefit in handheld ultrasound imaging with flexible configuration and can also serve as pre-research in other advanced real-time clinic applications.

REFERENCES

- [1] Y. Baribeau et al., "Handheld point-of-care ultrasound probes: The new generation of POCUS," *J. Cardiothoracic Vasc. Anesth.*, vol. 34, no. 11, pp. 3139–3145, 2020.
- [2] J. L. Díaz-Gómez, P. H. Mayo, and S. J. Koenig, "Point-of-care ultrasonography," *New England J. Med.*, vol. 385, pp. 1593–1602, 2021.
- [3] N. Cardim et al., "The use of handheld ultrasound devices: A position statement of the European association of cardiovascular imaging (2018 update)," *Eur. Heart J.: Cardiovasc. Imag.*, vol. 20, pp. 245–252, 2019.
- [4] L. J. Brattain et al., "AI-enabled, ultrasound-guided handheld robotic device for femoral vascular access," *Biosensors*, vol. 11, 2021, Art. no. 522.
- [5] P. R. Coombs, M. Warsa, T. Hailu, E. Agedew, and B. Tsegaye, "Establishing an ultrasound screening protocol for chronic liver disease with a handheld device: A pilot project in Southern Ethiopia," *Ultrasound Med. Biol.*, vol. 48, pp. 702–710, 2022.
- [6] O. Asikha et al., "The accuracy of handheld ultrasound in the evaluation of symptomatic pregnant patients in the emergency department," *Ann. Emerg. Med.*, vol. 80, 2020, Art. no. s151.
- [7] Q. Huang, J. Zhou, and Z. Li, "Review of robot-assisted medical ultrasound imaging systems: Technology and clinical applications," *Neurocomputing*, vol. 559, 2023, Art. no. 126790.
- [8] M. Lin et al., "A fully integrated wearable ultrasound system to monitor deep tissues in moving subjects," *Nat. Biotechnol.*, vol. 42, pp. 448–457, 2024.
- [9] C. Wang et al., "Bioadhesive ultrasound for long-term continuous imaging of diverse organs," *Science*, vol. 377, pp. 517–523, 2022.
- [10] M. Abdullah-Al-Wadud, M. Hasanul Kabir, M. Ali Akber Dewan, and O. Chae, "A dynamic histogram equalization for image contrast enhancement," *IEEE Trans. Consum. Electron.*, vol. 53, pp. 593–600, May 2007.
- [11] J. L. Mateo and A. Fernández-Caballero, "Finding out general tendencies in speckle noise reduction in ultrasound images," *Expert Syst. with Appl.*, vol. 36, pp. 7786–7797, 2009.
- [12] C. Dong, C. C. Loy, K. He, and X. Tang, "Learning a deep convolutional network for image super-resolution," in *Proc. Eur. Conf. Comput. Vis.*, 2014, pp. 184–199.
- [13] D. Li and Z. Wang, "Video superresolution via motion compensation and deep residual learning," *IEEE Trans. Comput. Imag.*, vol. 3, pp. 749–762, Dec. 2017.
- [14] Z. Zhou, Y. Guo, and Y. Wang, "Handheld ultrasound video high-quality reconstruction using a low-lank representation multipathway generative adversarial network," *IEEE Trans. Neural Netw. Learn. Syst.*, vol. 32, no. 2, pp. 575–588, Feb. 2021.
- [15] J. Kang, C. Yoon, J. Lee, S. B. Kye, Y. Lee, and J. H. Chang, "A system-on-chip solution for point-of-care ultrasound imaging systems: Architecture and ASIC implementation," *IEEE Trans. Biomed. Circuits Syst.*, vol. 10, no. 2, pp. 412–423, Apr. 2016.
- [16] D. Hyun, Y. L. Li, I. Steinberg, M. Jakovljevic, T. Klap, and J. J. Dahl, "An open source GPU-based beamformer for real-time ultrasound imaging and applications," in *Proc. IEEE Int. Ultrasonics Symp.*, 2019, pp. 20–23.
- [17] Z. Kou et al., "High-level synthesis design of scalable ultrafast ultrasound beamformer with single FPGA," *IEEE Trans. Biomed. Circuits Syst.*, vol. 17, pp. 446–457, Jun. 2023.
- [18] B. Jana, R. Biswas, P. K. Nath, G. Saha, and S. Banerjee, "Smartphone-based point-of-care system using continuous-wave portable doppler," *IEEE Trans. Instrum. Meas.*, vol. 69, pp. 8352–8361, Oct. 2020.
- [19] L. Willems et al., "Construct validity and reproducibility of handheld ultrasound devices in carotid artery diameter measurement," *Ultrasound Med. Biol.*, vol. 49, pp. 866–874, 2023.
- [20] H. Lee, H. Y. Sohn, C. Yoon, Y. Yoo, and T. K. Song, "Softwarebased hand-held ultrasound color doppler imaging system," in *Proc. IEEE Int. Ultrasonics Symp.*, 2009, pp. 1844–1847.
- [21] C. H. Hu, Q. Zhou, and K. K. Shung, "Design and implementation of high frequency ultrasound pulsed-wave doppler using FPGA," *IEEE Trans. Ultrasonics, Ferroelectr., Freq. Control*, vol. 55, no. 9, pp. 2109–2111, Sep. 2008.
- [22] C. C. Huang, P. Y. Lee, P. Y. Chen, and T. Y. Liu, "Design and implementation of a smartphone-based portable ultrasound pulsed-wave doppler device for blood flow measurement," *IEEE Trans. Ultrasonics, Ferroelectr., Freq. Control*, vol. 59, no. 1, pp. 182–188, Jan. 2012.
- [23] G. Peyton, B. Farzaneh, H. Soleimani, M. G. Boutelle, and E. M. Drakakis, "Quadrature synthetic aperture beamforming front-end for miniaturized ultrasound imaging," *IEEE Trans. Biomed. Circuits Syst.*, vol. 12, no. 4, pp. 871–883, Aug. 2018.
- [24] B. L. West, J. Zhou, R. G. Dreslinski, O. D. Kripfgans, J. B. Fowlkes, and C. Chakrabarti, "Tetris: Using software/hardware co-design to enable handheld, physics-limited 3D plane-wave ultrasound imaging," *IEEE Trans. Comput.*, vol. 69, pp. 1209–1220, Aug. 2020.
- [25] A. Ibrahim, P. A. Hager, A. Bartolini, F. Angiolini, M. Arditì, and J. P. Thrian, "Efficient sample delay calculation for 2-D and 3-D ultrasound imaging," *IEEE Trans. Biomed. Circuits Syst.*, vol. 11, no. 4, pp. 815–831, Aug. 2017.
- [26] G.-D. Kim et al., "A single FPGA-based portable ultrasound imaging system for point-of-care applications," *IEEE Trans. Ultrasonics, Ferroelectr., Freq. Control*, vol. 59, pp. 1386–1394, Jul. 2012.
- [27] J. U. Kidav, N. M. Sivamangai, M. P. Pillai, and R. M. S., "Architecture and FPGA prototype of cycle stealing DMA array signal processor for ultrasound sector imaging systems," *Microprocessors Microsystems*, vol. 64, pp. 53–72, 2019.
- [28] H. T. Feldkamper, R. Schwann, V. Gierenz, and T. G. Noll, "Low power delay calculation for digital beamforming in handheld ultrasound systems," in *Proc. IEEE Ultrasonics Symp.*, 2000, vol. 2, pp. 1763–1766.
- [29] P. A. Hager, D. Speicher, C. Degel, and L. Benini, "UltraLight: An ultrafast imaging platform based on a digital 64-channel ultrasound probe," in *Proc. 2017 IEEE Int. Ultrasonics Symp.*, 2017, pp. 1–5.
- [30] A. Perez-Sanchez et al., "Comparison of 6 handheld ultrasound devices by point-of-care ultrasound experts: A cross-sectional study," *Ultrasound J.*, vol. 16, no. 1, pp. 45, 2024.
- [31] A. Rykkje, J. F. Carlsen, and M. B. Nielsen, "Hand-held ultrasound devices compared with high-end ultrasound systems: A systematic review," *Diagnostics*, vol. 9, no. 2, 2019, Art. no. 61.
- [32] Y. Zhang et al., "A low-voltage-driven MEMS ultrasonic phased-array transducer for fast 3D volumetric imaging," *Microsyst. Nanoeng.*, vol. 10, 2024, Art. no. 128.
- [33] Z. Rong, M. Zhang, Y. Ning, and W. Pang, "An ultrasound-induced wireless power supply based on AlN piezoelectric micromachined ultrasonic transducers," *Sci. Rep.*, vol. 10, 2022, Art. no. 16174.
- [34] J. Wang, Z. Zheng, J. Chan, and J. T. W. Yeow, "Capacitive micromachined ultrasound transducers for intravascular ultrasound imaging," *Microsystems Nanoeng.*, vol. 6, 2020, Art. no. 73.